Bone 60 (2014) 172–185

Contents lists available at ScienceDirect

Bone

journal homepage: www.elsevier.com/locate/bone

Original Full Length Article

3D osteocyte lacunar morphometric properties and distributions in human femoral cortical bone using synchrotron radiation micro-CT images

Pei Dong [a,b,*], Sylvain Haupert [c], Bernhard Hesse [a,b,d], Max Langer [a,b], Pierre-Jean Gouttenoire [a,b], Valérie Bousson [e], Françoise Peyrin [a,b]

[a] CREATIS, CNRS UMR 5220; Inserm U1044; Université de Lyon; Université Lyon 1; INSA-Lyon, 69621 Villeurbanne, France
[b] European Synchrotron Radiation Facility, X-Ray Imaging Group, 38043 Grenoble, France
[c] UMPC Univ Paris 6, UMR 7623, Laboratoire d'Imagerie Paramétrique, 75006 Paris, France
[d] Berlin-Brandenburg School for Regenerative Therapies, Charité-Universitätsmedizin Berlin, Berlin, Germany
[e] Univ Paris Diderot, Sorbonne Paris Cité, B2OA, UMR 7052 CNRS, 75010 Paris, France

ARTICLE INFO

Article history:
Received 24 June 2013
Revised 26 November 2013
Accepted 4 December 2013
Available online 12 December 2013

Edited by: David Fyhrie

Keywords:
Osteocyte lacunae
Synchrotron radiation micro-CT
3D image analysis
Lacunar descriptors
Cortical bone

ABSTRACT

Osteocytes, the most numerous bone cells, are thought to be actively involved in the bone modeling and remodeling processes. The morphology of osteocyte is hypothesized to adapt according to the physiological mechanical loading. Three-dimensional micro-CT has recently been used to study osteocyte lacunae. In this work, we proposed a computationally efficient and validated automated image analysis method to quantify the 3D shape descriptors of osteocyte lacunae and their distribution in human femurs. Thirteen samples were imaged using Synchrotron Radiation (SR) micro-CT at ID19 of the ESRF with 1.4 μm isotropic voxel resolution. With a field of view of about 2.9 × 2.9 × 1.4 mm^3, the 3D images include several tens of thousands of osteocyte lacunae. We designed an automated quantification method to segment and extract 3D cell descriptors from osteocyte lacunae. An image moment-based approach was used to calculate the volume, length, width, height and anisotropy of each osteocyte lacuna. We employed a fast algorithm to further efficiently calculate the surface area, the Euler number and the structure model index (SMI) of each lacuna. We also introduced the 3D lacunar density map to directly visualize the lacunar density variation over a large field of view. We reported the lacunar morphometric properties and distributions as well as cortical bone histomorphometric indices on the 13 bone samples. The mean volume and surface were found to be 409.5 ± 149.7 μm^3 and 336.2 ± 94.5 μm^2. The average dimensions were of 18.9 ± 4.9 μm in length, 9.2 ± 2.1 μm in width and 4.8 ± 1.1 μm in depth. We found lacunar number density and six osteocyte lacunar descriptors, three axis lengths, two anisotropy ratios and SMI, that are significantly correlated to bone porosity at a same local region.
The proposed method allowed an automatic and efficient direct 3D analysis of a large population of bone cells and is expected to provide reliable biological information for better understanding the bone quality and diseases at cellular level.

Introduction

Intensive studies have been carried out over the last decades to explain the bone fragility in diseases such as osteoporosis. Bone mass measurement has proved to be a valuable parameter in the evaluation of bone fragility. However, bone mass could explain only a fraction of change in bone strength among individuals [1]. Other factors known as bone quality factors are believed to have an impact on bone mechanical properties [2]. They include both bone microstructure and the materials properties of bone tissue at different scales.

At the cellular scale, the osteocyte system is raising increasing interest since it is hypothesized to have an important role in bone adaptation to stresses [3,4]. The osteocytes, which represent about 90% of the bone cells are the mechanosensory cells that translate mechanical stimuli into electrical or biochemical signals and orchestrate the osteoclasts and the osteoblasts to perform bone resorption and formation [5–7]. The osteocytes also regulate bone metabolism, for example bone phosphate metabolism [8], and were recently shown to remodel their pericanalicular matrix [9]. However, the exact mechanisms involved in the osteocytes activity are not precisely elucidated and remain controversial.

* Corresponding author at: CREATIS–INSA LYON, Bâtiment Blaise Pascal (4ème étage), 7 Avenue Jean Capelle, 69621 Villeurbanne Cedex, France. Fax: +33 476882252.
E-mail addresses: Pei.Dong@creatis.insa-lyon.fr (P. Dong), sylvain.haupert@upmc.fr (S. Haupert), bernhard.hesse@esrf.fr (B. Hesse), max.langer@esrf.fr (M. Langer), goutteno@esrf.fr (P.-J. Gouttenoire), valerie.bousson@lrb.aphp.fr (V. Bousson), peyrin@esrf.fr (F. Peyrin).

8756-3282/$ – see front matter © 2013 Elsevier Inc. All rights reserved.
http://dx.doi.org/10.1016/j.bone.2013.12.008

Osteocytes have been less studied than osteoblasts and osteoclasts, partly because of their anatomical location [4]. While osteoblasts and osteoclasts are performing their duties on the surface of bone, the osteocytes are deeply embedded in the bone matrix. The latter are encysted in cavities called lacunae, and they connect to each other and to bone cells at surface through slender dendritic processes located in tunnels called canaliculi. The geometry of the lacuno-canalicular network (LCN) is believed to affect the magnitude of bone fluid shear stress loaded on the osteocyte [10–12], which in turns affect the process of mechanosensation and mechanotransduction [7]. We believe that a better investigation on the morphology of LCN will lead to a better understanding of bone tissue regulation and bone mechanical properties at the cell level.

Direct observation of osteocytes is difficult and there are relatively few quantitative data on their morphology [13]. In the past, osteocytes were mainly examined using microscopic modalities such as light microscopy [14], confocal microscopy [15,16], scanning electron microscopy (SEM) [17,18] and transmission electron microscopy (TEM) [19,20]. These techniques provide only 2D observations or are limited to at most several hundreds of micrometers in depth. To overcome this limitation, several 3D imaging techniques have recently been proposed. Novel 3D imaging techniques, such as focused ion beam/scanning electron microscopy (FIB/SEM) [21] and ptychography [22] look promising for very high resolution imaging of the LCN, but remain limited to the analysis of one or a few osteocyte lacunae. Recently, the feasibility of commercialized nano-CT was also demonstrated to visualize the 3D morphology of osteocyte lacunae [16,23]. Coupling micro-CT to synchrotron sources (SR) permits the use of parallel monochromatic high flux X-ray beams. Thus, SR micro-CT possesses several advantages over conventional desktop micro-CT in terms of signal to noise ratio, spatial and density resolution [24]. Moreover, due to the high brilliance source, the acquisition time is considerably reduced. Early 3D observations of osteocyte lacunae in trabecular bone were reported with SR micro-CT at a spatial resolution around the micrometer [13,25,26]. More recently, quantitative properties of osteocyte lacunae in the midshaft of human femoral cortical bone were measured from SR micro-CT images [27,28].

Quantitative morphometric data on osteocytes or osteocyte lacunae were mostly obtained from 2D images, most of the time by manual measurements. Osteocyte lacunae are typically described as flattened ellipsoids [29] with a size of a few micrometers. They were reported to have a long and a short axis respectively about 20 and 9 μm from 2D microscopic images [30]. However, when observed from 2D sections, there may be incertitude in their actual 3D dimensions due to the slicing direction. Although geometric models for the osteocytes have been established to extrapolate the 2D measurements to 3D quantitative values [30–32], this method can lead to unpredictable errors if these ideal model assumptions are not verified. Since some results could turn out to be contradictory [33], direct 3D measurements are required to get unbiased results.

Such 3D morphometric data on osteocyte lacunae were first obtained with confocal microscopy. McCreadie [33] provided a method to evaluate osteocyte lacunar shape and size in 3D among 600 lacunae. However, this imaging modality presents some inherent artifacts impacting quantification. First, the lower spatial resolution in depth may yield inaccuracies. Second, the limited field of view (FOV) in depth also restricts the region of interest. Besides, since the osteocyte lacunae are deeply embedded in the bone matrix, some osteocyte lacunae may be lost during the staining process, thus yielding to an underestimation of lacunar density. Micro and nano-CT imaging overcome these drawbacks and provide 3D images with isotropic voxels without requiring staining. Van Hove [16] and Vatsa [23] measured lacunar volume, surface area, degree of anisotropy from the SkyScan nano-CT device. Recently, Hannah [27] reported morphometric parameters, such as volume, long axis length and orientation angle, and mean nearest neighbor distance in 11 non-branched osteons from SR micro-CT images. He observed a bimodal distribution of osteocyte lacunar size in human femoral cortex [27]. Carter [28] reported volume, orientation, equancy, elongation, and flatness of osteocyte lacuna at different locations in one healthy male femur. He reported that lacunae were more flattened in the anterior and posterior regions than in the medial and lateral regions. Nevertheless, in the previous works, there has not been a lot of focus on the method to extract lacunar descriptors, neither in its description nor on its validation, and the numbers of samples and subjects analyzed so far, were quite limited.

The aim of this work is to describe a clear and reproducible methodology to quantify large population of osteocyte lacunae and report new data on human cortical bone samples to improve our knowledge about the 3D properties of osteocyte lacuna in human bone. Our approach was (1) to use SR micro-CT at 1.4 μm, a good candidate for imaging such a network since it provides images with isotropic voxel size over large FOV ($2.9 \times 2.9 \times 1.4\ mm^3$) allowing to enclose between 10^5 and 10^6 cells [28], (2) to develop a fast and efficient image analysis method for the automatic quantification of the 3D cell morphometry, (3) to extract reliable statistical morphological descriptors from 13 samples in human midshaft cortical bone and look for correlations between those descriptors and bone porosity.

Material and methods

Sample description

Thirteen human cortical bone specimens were prepared from the femoral mid-diaphysis of two female donors (seven specimens from donor A with death age of 78 years and six specimens from donor B with death age of 80 years). Ethical approval for the collection of samples was granted by the Human Ethics Committee of the Centre du don des Corps at the University Paris Descartes (Paris, France). Informed written consent was signed by the donors or their legal guardians to provide the tissue for investigation in accordance with legal clauses stated in the French Code of Public Health. The specimens were wet machined (Isomet 4000, Buehler GmbH, Düsseldorf, Germany) as parallelepiped beams ($50 \times 4 \times 2\ mm^3$), defatted [34] and stored at −20 °C until experiments.

Synchrotron radiation microtomography (SR-μCT)

SR micro-CT was performed on beamline ID19 at the ESRF (European Synchrotron Radiation Facility, Grenoble, France). For each sample, 3000 projection images were recorded over a total angle of 360° at a fixed energy of 25 keV. A 3D image volume with an isotropic spatial resolution of 1.4 μm was reconstructed by a filtered back-projection algorithm. To decrease the computational burden and to avoid geometrical distortion at the periphery of the image, a volume of interest (VOI) was selected with size of $1000 \times 1000 \times 251$ voxels, which corresponds to a physical size of 1.4 mm × 1.4 mm × 0.35 mm (see Fig. 1(a)). Fig. 1(b) illustrates a reconstructed slice from the VOI, the light gray part of the images corresponds to mineralized cortical bone. The large black pores are cross sections of Haversian canals and Volkmann's canals. Fig. 1(c) shows a zoom around on an osteon, where the small black cavities scattered around the Haversian canal on the gray background are osteocyte lacunae.

Image processing

The method was developed to extract parameters at two levels, the cell level and the tissue level. At the cell level, we calculated the three-dimensional descriptors on individual cells: length (*Lc.L1*), width (*Lc.L2*), depth (*Lc.L3*), anisotropy, surface area (*Lc.S*), Euler number ($Lc.\chi$), structure model index (*Lc.SMI*). At the tissue level, we quantified the following parameters: bone volume fraction (*BV/TV*), canal volume fraction (*Ca.V/TV*), and the number and volume of osteocyte lacunae

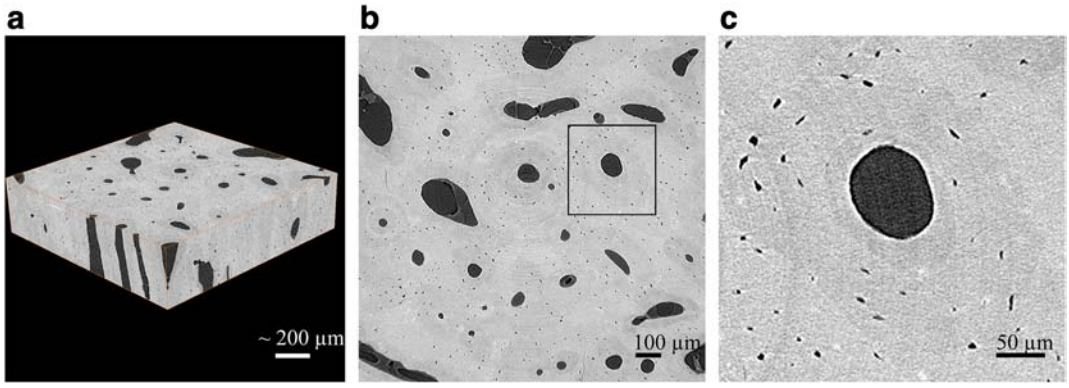

Fig. 1. (a) A 3D rendering of the reconstructed image (1000 × 1000 × 251 pixels). (b) A slice of reconstructed image from SR-CT with voxel resolution of 1.4 μm (image size: 1000 × 1000 pixels). (c) Zoom around a Haversian canal.

(*N.Lc* and *Lc.TV*) and its 3D density. Furthermore, properties characterizing the distance of the mineralized matrix to canals and lacunae were computed. To obtain these parameters, the following steps were performed.

Segmentation of osteocyte lacunae

First, by using a Gaussian low pass filter and a simple thresholding, it was straightforward to acquire a mask volume including the bone cortex and excluding the canals, Fig. 2(a). This mask volume was further used to calculate the bone volume (*BV*). Then, to segment the osteocyte lacunae within the region of the mask volume, a hysteresis thresholding with two thresholds was employed [35]. The first lower threshold was used to select the voxels belonging to osteocyte lacunae with a high confidence. Then a second higher threshold was used to refine the segmentation by selecting the voxels with higher intensity values but only if they were connected to the previously detected voxels. After rescaling the reconstructed images between 0 and 255, the segmentation of lacunae was achieved by setting the two hysteresis thresholds respectively to 40 and 70. As a result, a binary volume of osteocyte lacunae was acquired Fig. 2(b).

Labeling, number of lacunae (N.Lc)

To quantify each individual cell, a connected component process was first performed to assign a label to each of them. Considering the large dimensions of the 3D images to be processed, an efficient labeling method was chosen. Hoshen and Kopelmanm proposed a fast labeling algorithm for 2D images requiring scanning the image only twice [36]. We extended and implemented this algorithm for labeling 3D images. In this work, the labeling was performed with a connectivity of 26 (meaning that each voxel was connected to its 26 3D neighbors). Fig. 2(c) illustrates some labeled osteocyte lacunae around an osteon. After labeling, all lacunae connected to the image borders were deliberately erased from the labeled volume to avoid biasing the results that could be related to truncated lacunae. The total number of labels corresponds to the number of lacunae and is denoted *N.Lc*.

Calculation of 3D individual osteocyte lacunar descriptors

At the cell level, a number of descriptors were calculated for each labeled lacuna. Let $L(x,y,z)$ be the labeled image where (x,y,z) are the spatial coordinates belonging to a finite domain of $\mathbb{N}^3$. Let X_n denote the nth labeled osteocyte lacuna composed of the set of voxels labeled as n. We extracted two classes of descriptors, respectively associated to second order moments and intrinsic volumes.

Volume of lacuna (Lc.V)

The volume of lacuna X_n is denoted $Lc.V(X_n)$ and can be simply obtained by counting the number of voxels labeled as n.

Distance distribution of lacunae, $Lc.Dist_{50}$ $Lc.Dist_{95}$

The distribution of the distance map of the lacunae was used to explore their spatial arrangement [37]. It depicts what is the distance of the bone matrix from the nearest osteocyte lacuna, denoted as *Lc.Dist*. First, we calculated the distance map of binary lacunae image, giving at each bone voxel its shortest distance to the surface of the nearest osteocyte lacuna. Second, the normalized cumulative histogram of the distance map is calculated. Finally, the values corresponding to 50% and 95% of the distribution, denoted as $Lc.Dist_{50}$ and $Lc.Dist_{95}$, are determined. The two calculated parameters show that 50% and 95% of the

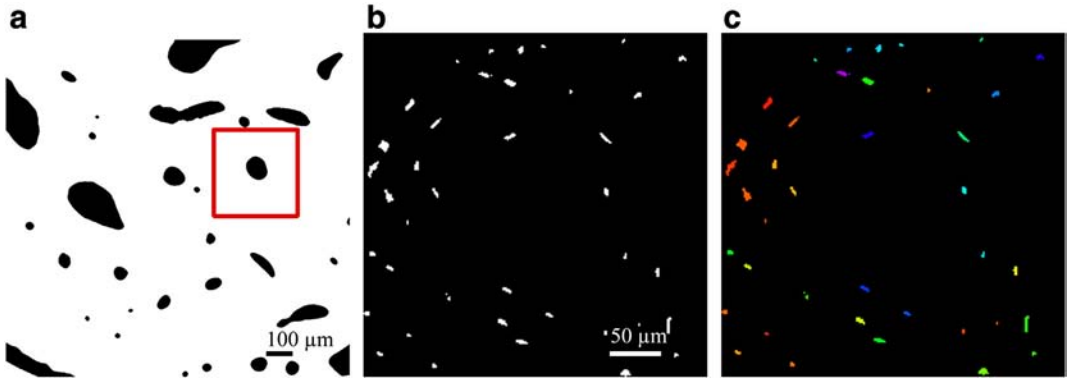

Fig. 2. (a) A slice of bone matrix mask. (b) Binary segmented osteocyte lacunae around an osteon. (c) Labeled osteocyte lacunae around an osteon.

bone matrix are located within a distance of $Lc.Dist_{50}$ and $Lc.Dist_{95}$ from the nearest lacunae.

Moment based descriptors, length (Lc.L1), width (Lc.L2), depth (Lc.L3), and anisotropy

Since the shape of osteocyte lacunae is generally assumed to be ellipsoidal, second order moments can efficiently be used to find the main orientations and the lengths of the main axis of the best fitting ellipsoid. First, we defined the second-order central moments μ_{pqr} of X_n, with $p + q + r = 2$ for $(p,q,r) \in [0,2]$ given by:

$$\mu_{pqr} = \sum_{(x,y,z)\in X_n} (x-\overline{x}_n)^p \cdot (y-\overline{y}_n)^q \cdot (z-\overline{z}_n)^r \quad (1)$$

where the $(\overline{x}_n, \overline{y}_n, \overline{z}_n)$ is the center of mass of X_n.

The second order moment matrix can be expressed as:

$$M(X_n) = \begin{pmatrix} \mu_{200} & \mu_{110} & \mu_{101} \\ \mu_{110} & \mu_{020} & \mu_{011} \\ \mu_{101} & \mu_{011} & \mu_{002} \end{pmatrix} \quad (2)$$

Let $\lambda_1 \geq \lambda_2 \geq \lambda_3$ be the eigenvalues of $M(X_n)$. It can be shown that the half axes of the best fitting ellipsoid are:

$$a_k = \sqrt{5\lambda_k / Lc.V(X_n)}, \quad k = 1,2,3 \quad (3)$$

The sizes of the osteocyte lacunae sorted in descending order, that will be referred as length, width, and depth, can thus be given by:

$$Lc.L_1(X_n) = 2a_1, \quad Lc.L_2(X_n) = 2a_2, \quad Lc.L_3(X_n) = 2a_3 \quad (4)$$

The ratio between the volume of the actual osteocyte lacunae and the fitting ellipsoid is given by:

$$\tau = 3Lc.V(X_n)^{5/2} / 20\pi\sqrt{5\lambda_1\lambda_2\lambda_3} \quad (5)$$

The major orientation of the lacuna is given by that of the eigenvector associated to λ_1. The anisotropy of the lacunae can also be quantified by the ratios of axis lengths $Lc.L_1/Lc.L_2$ and $Lc.L_1/Lc.L_3$.

Intrinsic volumes based descriptors: surface area (Lc.S), Euler number (Lc.χ), structure model index (Lc.SMI)

To further quantify each object X_n, we calculated the surface area $Lc.S(X_n)$, the Euler number $Lc.\chi(X_n)$ and the structure model index (SMI) $Lc.SMI(X_n)$ of the lacuna X_n. The Euler number and SMI are geometric invariant features (i.e. features that are not modified by geometric transformations like translation, rotation and scaling) independent of the geometric size of the object, widely used in computer vision. The Euler number is used to depict the topological property of the lacuna. It is equal to the number of connected component minus the number of tunnels plus the number of cavities. The SMI [38] characterizes the lacunar shape with values of 0, for a pure plate, 3 for a rod and 4 for a sphere. The lacunar surface, Euler number and SMI were calculated from the intrinsic volumes $V_0(X_n)$, $V_1(X_n)$, $V_2(X_n)$ by applying Eq. (6) [39]. These intrinsic volumes, which are also geometric invariants, were computed by a fast algorithm basically requiring only one scan of the 3D volume to deduce the three quantities $V_0(X_n)$, $V_1(X_n)$, $V_2(X_n)$ (see [39–42] for details).

$$Lc.S(X_n) = 2V_2(X_n), \quad Lc.\chi(X_n) = V_0(X_n), \quad (6)$$

$$Lc.SMI(X_n) = 12\pi Lc.V(X_n)V_1(X_n)/Lc.S(X_n)^2$$

Calculation of tissue indices

At tissue level, bone histomorphometric indices were calculated. The bone volume (*BV*) was evaluated from the 3D mask image already used in the stage of lacunae segmentation. The tissue volume (*TV*) was obtained by taking the convex hull algorithm of the mask volume. The Haversian and Volkmann canals volume (*Ca.V*) was evaluated as TV minus BV. This allows evaluating the bone volume fraction *BV/TV*, the canal volume fraction *Ca.V/TV* or bone porosity. The total lacunar volume *Lc.TV* can be obtained either directly from the binary image of lacunae or by summing the individual volume of each lacunae. The lacunar number density, denoted as *N.Lc/BV* and *N.Lc/TV*, and the lacunar volume density, denoted as *Lc.TV/BV* and *Lc.TV/TV* was also calculated.

In addition, we also calculated the distance distribution of the Haversian canal. It depicts the average distance of the bone matrix from the nearest Haversian canal. First, we calculated the distance map of the binary Haversian canal image, giving at each bone voxel its shortest distance to the surface of the nearest Haversian canal. Second, the normalized cumulative histogram of the distance map is calculated. Finally, the values corresponding to 50% and 95% of the distribution, denoted as $Ca.Dist_{50}$ and $Ca.Dist_{95}$, are determined. The two calculated parameters represent that 50% and 95% of bone matrix are located within a distance of $Ca.Dist_{50}$ and $Ca.Dist_{95}$ from the nearest Haversian canal.

Artifacts elimination

The hysteresis thresholding provided a binary image but, as in every automatic segmentation method, there may be artifacts, for instance due to ring artifacts, micro-cracks or noise. These artifactual structures have different shapes than that expected for lacunae. Thus we took advantage of the descriptors calculated on each object to eliminate them. The objects with volume smaller than 82 μm^3 (30 voxels) were removed considered as noise. The objects, which volumes were within the top 1% of the distribution, were assumed to be artifactual lacunae, such as micro-cracks and canals, and were removed. Besides, the objects with an anisotropy ratio *Lc.L1/Lc.L2* larger than 5, which often appeared to be ring artifacts, were also eliminated. Furthermore, the 3D Euler number $Lc.\chi$ was exploited to control the topology of the structure. Finally, the rule applied to filter out artifactual components was the following

$$Lc.V > Lc.V \text{ within the top } 1\% \text{ and } Lc.V < 82\ \mu m^3; Lc.L1/Lc.L2 > 5; \quad Lc.\chi < 0 \text{ and } Lc.\chi > 2 \quad (7)$$

The method was evaluated by comparison to a semi-manual segmentation on a volume of interest made of 200^3 voxels in representative micro-CT image. To this aim, we used a semi-interactive process based on region growing. For each lacuna, we selected interactively a seed close to the center of gravity of the lacunae. Then a region growing starting from this seed was performed using MeVisLab (Version 2.1). The resulting binary image was overlapped with the original image using ImageJ (version 1.45 s). A manual refinement was performed on individual lacuna to achieve the ideal segmentation result by a manual modification on the binarized lacuna compared with the same lacuna in original image.

To compare the automatic segmentation with respect to the manually segmented image, we used the Dice coefficient, conventionally used in medical imaging and defined as twice the number of voxels common to both images by the sum of the voxels in each image [43]. An ideal segmentation corresponds to a Dice value of one. Sensitivity and specificity were calculated as well. We also compared the descriptors extracted from the automatic and manually segmented images.

Local analysis

Qualitative analysis

In order to study the lacunar density variation with respect to the bone porosity, we introduced a 3D lacunar density map. First, we calculated a local lacunar density *N.Lc(r)/BV(r)* at the gravity center of each

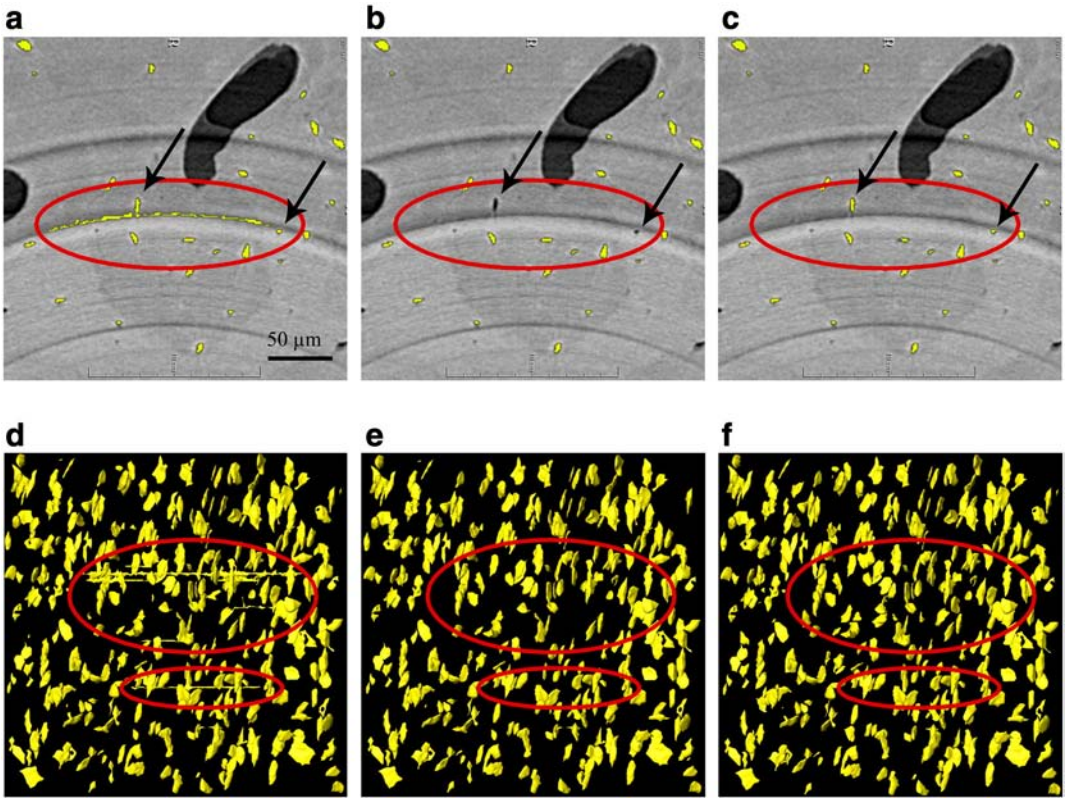

Fig. 3. Comparison of before and after artifact elimination with the reference image. (a) Before artifact elimination. (b) After artifact elimination. (c) Reference image. (d)–(e) The corresponding results of (a)–(c) in 3D.

lacuna. This parameter was calculated in a local region which was defined by a bounding box with length of $2r + 1$ voxels. The number of lacunae *N.Lc(r)* and the bone volume *BV(r)* were calculated within the local region. After that, each lacuna was labeled with the value of the local density. The 3D local lacunar density map gives a 3D image, the intensity of which represented the local lacunar density. It was used to visually identify the local regions with high or low lacunar density.

This analysis was performed on two of the thirteen samples. Since the density analysis is not sensitive to the shape of lacunae, a larger VOI ($1000 \times 1500 \times 261$ voxels) was cropped from the reconstructed 3D image. Minimum intensity projections of these two samples are shown in Figs. 6(a) and (b). It can be clearly seen that in one sample there are large variations of bone porosity, while the second one is quite homogenous. To calculate the 3D lacunar density map, we used a region of 22.28×10^{-3} mm^3 ($r = 140$ μm) around each lacunar gravity center, which is appropriate to reflect the density variation across the whole region of interest.

Quantitative analysis

To quantitatively evaluate the relationships between local bone porosity and lacunar density and descriptors, the sample, containing variations of local bone porosity, was divided into seven sub-volumes with size of $300 \times 1500 \times 261$ voxels. Each of them owns different bone volume fraction (*BV/TV*) ranging from 67% to 97% (Fig. 7). The lacunae were segmented, and the artifacts were eliminated according to Eq. (7). Besides bone volume fraction (*BV/TV*), lacunar density (*N.Lc/BV*), axes length (*Lc.L1*, *Lc.L2*, *Lc.L3*), anisotropy (*Lc.L1/Lc.L2*, *Lc.L1/Lc.L3*), structural model index (*Lc.SMI*), volume (*Lc.V*) and surface (*Lc.S*) of osteocyte lacunae were calculated from each sub-volume.

Statistics analysis

Descriptive statistics were used to describe the features on the quantification result of the thirteen samples. For the local quantitative analysis, we used StatView® 5.0 to perform the linear regression analysis between bone porosity and lacunar descriptors extracted from the seven sub-volumes. F-test was used to check the significance of the overall fit, followed by *t*-test on the significance of slope and intercept. The significance level was measured using a p-value $p < 0.05$.

Results

Evaluation of the segmentation method

From a visual point of view, the hysteresis method seemed to perform well. However a more detailed observation revealed the presence of artifacts. Figs. 3(a) and (d) respectively illustrate a 3D rendering and an overlay of a reconstructed slice and the result of hysteresis thresholding. Ring artifacts are visible on both displays. Figs. 3(b) and (e) show the same images after artifact elimination, showing that the ring artifacts have successfully been eliminated. Figs. 3(c) and (f)

Table 1
Segmentation validation.

Descriptor	Segmentation	Reference image	Ratio	DICE	Sensitivity	Specificity
N.Lc	328	357	91.9%	94.57%	92.10%	99.98%
Lc.V(μm^3)	357.36	350.66	98.1%			
Lc.S(μm^2)	314.66	308.16	97.9%			
Lc.L1 (μm)	18.46	18.04	97.7%			
Lc.L2 (μm)	9.08	9.02	99.3%			
Lc.L3 (μm)	4.70	4.64	98.7%			
Lc.L1/Lc.L2	2.16	2.12	98.1%			
Lc.L1/Lc.L3	4.17	4.13	98.8%			

N.Lc—number of lacunae.
Lc.V—lacunar volume (μm^3).
Lc.S—lacunar surface area (μm^2).
Lc.L1, Lc.L2 and Lc.L3—length, width and depth of lacuna (μm).
Lc.L1/Lc.L2 and Lc.L1/Lc.L3—anisotropy of lacuna.

present the semi-manually segmented images, which look close to the final segmentation result. The quantitative evaluation of the method is reported in Table 1. The Dice coefficient reflected a satisfactory segmentation compared with the reference image. The ratios of the main descriptors were above 98% which indicate highly reliable statistical results. There were about 8% of cells missing after segmentation. This was mainly due to the loss of the cells which were connected to the artifacts.

Figs. 4(a) and (b) show a top and a side 3D view of one of the subvolume, with the Haversian and Volkmann canals and the segmented lacunae. From Fig. 4(a), the osteocyte lacunae can be clearly recognized as they were distributed in concentric circles around the Haversian canals. Fig. 4(c) shows a zoom around one osteon. By using the tensor field visualization rendered by Avizo® (version 6.1), it was possible to visualize the best fitting ellipsoid of each osteocyte lacunae calculated from the second order matrix (Fig. 4(d)). This display shows that the fitting was in agreement with the original data.

Histomorphometry parameters of the bone tissue

Table 2 reports the descriptive statistics features of the bone tissue. Of the thirteen samples, the average number of lacunae was 12,791, with the total lacunar volume of 0.013 mm^3. The bone volume fraction (*BV/TV*) and canal volume fraction (*Ca.V/TV*) are of 89.6% ± 9.3% and 10.4% ± 9.3%. The average and standard deviation of lacunar number densities were 20,573 ± 2850/mm^3 (*N.Lc/BV*) and 18572 ± 3675/mm^3 (*N.Lc/TV*). The lacunar volume densities were 0.84% ± 0.17% (*Lc.TV/BV*) and 0.76% ± 0.19% (*Lc.TV/TV*). The 50% and 95% of bone voxels are located within a distance of 64.6 ± 7.9 μm and 134.2 ± 12.5 μm from the nearest Haversian canal.

3D shape descriptors of osteocyte lacunae

Table 3 reports the descriptive statistics features of the osteocyte lacunar descriptors. The average lacunar volume was 409.5 ± 149.7 μm^3. The lacunar surface was 336.2 ± 94.5 μm^2. With the length of 18.9 ± 4.9 μm and the width of 9.2 ± 2.1 μm and the depth of 4.8 ± 1.1 μm, the average anisotropy (length: width: depth) of the osteocyte lacuna was approximately 4:2:1. The average and standard deviation of ratio (τ) between the volume of the actual osteocyte lacunae and the fitting ellipsoid was around 93.1% ± 6.6%. The lacunar structural model index was 3.3 ± 0.3. The 50% and 95% of bone voxels are located within a distance of 13.8 ± 1.0 μm and 27.5 ± 2.5 μm from the nearest lacuna. Besides, we also calculated the orientation of each lacuna. The results showed that the main direction of each cell was mainly in the direction of the Haversian channels. Fig. 5 illustrates the distributions of lacunar descriptors over 13 samples.

Osteocyte lacunar density distribution

To visualize the lacunar density variation, Figs. 6(c) and (d) show the 3D local lacunar density maps of the two samples. It appeared that

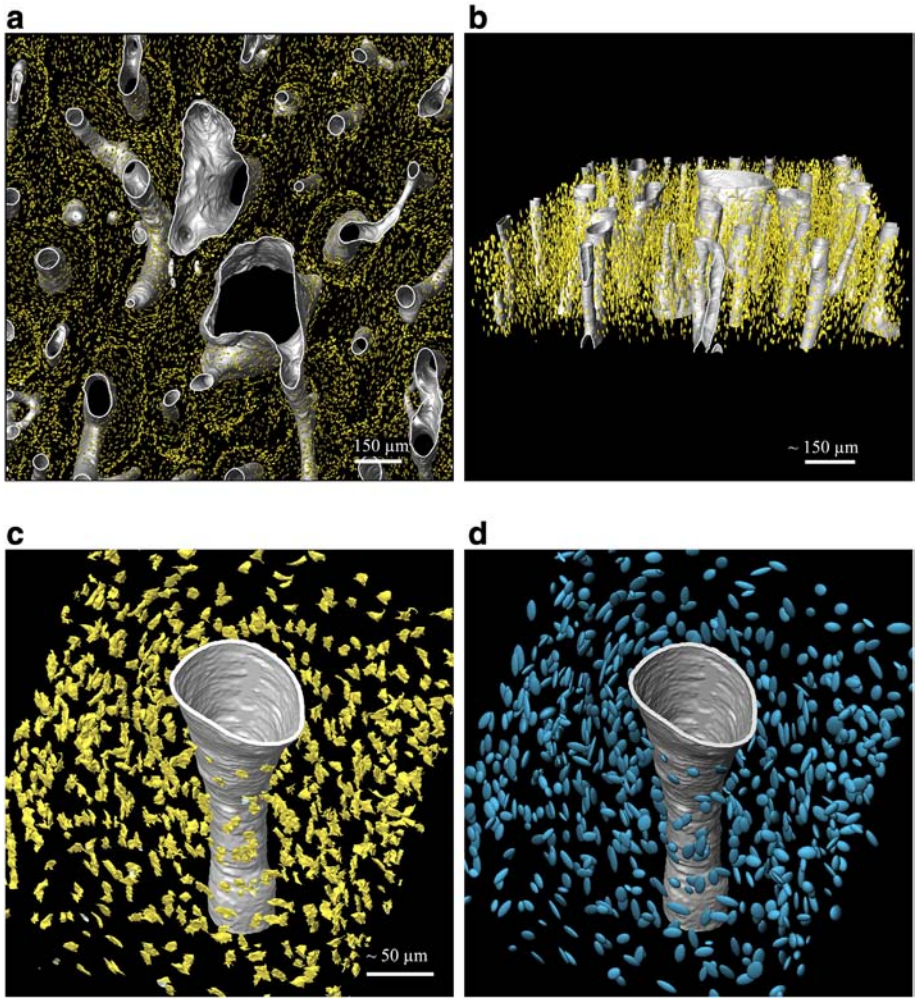

Fig. 4. 3D rendering of segmented image (1000 × 1000 × 251) (rendered by Avizo v6.1) (a) (b) Top view and side view of the volume. The Harversian canal (white) is surrounded by osteocyte lacunae (yellow) (c) A 3D rendering of an osteon (d) A corresponding 3D rendering of (c) with equivalent ellipsoids of osteocyte lacunae. (For interpretation of the references to color in this figure legend, the reader is referred to the web version of this article.)

Table 2
Histomorphometry parameters of the bone tissue from 13 specimens.

Sample ID	N.Lc	Lc.TV (mm^3)	BV (mm^3)	TV (mm^3)	BV/TV (%)	Ca.V/TV (%)	Lc.TV/BV (%)	Lc.TV/TV (%)	N.Lc/BV (mm^3)	N.Lc/TV (mm^3)	$Ca.Dist_{50}$ (μm)	$Ca.Dist_{95}$ (μm)
A1	12,177	0.0054	0.59	0.69	86.4%	13.6%	0.91%	0.79%	20,471	17680	58.8	123.2
A2	13,673	0.0055	0.65	0.69	94.6%	5.4%	0.85%	0.80%	20,981	19852	60.2	120.4
A3	10,851	0.0046	0.57	0.69	82.4%	17.6%	0.82%	0.67%	19,122	15755	56.0	114.8
A4	12,578	0.0046	0.63	0.69	92.1%	7.9%	0.72%	0.67%	19,836	18262	61.6	138.6
A5	16,808	0.0069	0.62	0.69	89.9%	10.1%	1.11%	1.00%	27,155	24404	60.2	128.8
A6	13,613	0.0048	0.63	0.69	91.5%	8.5%	0.76%	0.70%	21,607	19765	64.4	128.8
A7	16,449	0.0083	0.67	0.69	97.8%	2.2%	1.23%	1.20%	24,429	23883	79.8	155.4
B1	6499	0.0025	0.43	0.69	62.6%	37.4%	0.58%	0.36%	15,084	9436	50.4	123.2
B2	13,505	0.0052	0.67	0.69	96.8%	3.2%	0.77%	0.75%	20,259	19608	68.6	134.4
B3	12,477	0.0054	0.67	0.69	96.9%	3.1%	0.80%	0.78%	18,693	18116	72.8	144.2
B4	11,913	0.0049	0.60	0.69	87.2%	12.8%	0.81%	0.71%	19,839	17297	68.6	149.8
B5	13,477	0.0051	0.66	0.69	95.7%	4.3%	0.77%	0.74%	20,445	19568	67.2	134.4
B6	12,266	0.0049	0.63	0.69	91.2%	8.8%	0.79%	0.72%	19,528	17809	71.4	148.4
Mean A	13,736	0.0057	0.62	0.69	90.7%	9.3%	0.92%	0.83%	21,943	19943	63.0	130.0
Std.A	2195	0.0014	0.04	0.00	5.1%	5.1%	0.19%	0.20%	2856	3187	7.8	13.5
Mean B	11,690	0.0047	0.61	0.69	88.4%	11.6%	0.76%	0.68%	18,975	16972	66.5	139.1
Std.B	2624	0.0011	0.09	0.00	13.2%	13.2%	0.09%	0.15%	2004	3810	8.2	10.2
Mean.All	12791	0.0052	0.62	0.69	89.6%	10.4%	0.84%	0.76%	20,573	18572	64.6	134.2
Std.All	2531	0.0013	0.06	0.00	9.3%	9.3%	0.17%	0.19%	2850	3675	7.9	12.5

N.Lc—number of osteocyte lacunae.
Lc.TV—total lacunar volume (mm^3).
BV—bone volume (mm^3).
TV—tissue volume (mm^3).
BV/TV—bone volume fraction (%).
Ca.V/TV—canal volume fraction or bone porosity (%).
Lc.TV/BV and Lc.TV/TV—lacunar volume density (mm^{-3}).
N.Lc/BV and N.Lc/TV—lacunar number density (mm^{-3}).
$Ca.Dist_{50}$—average distance of 50% of bone matrix to the nearest Haversian canal (μm).
$Ca.Dist_{95}$—average distance of 95% of bone matrix to the nearest Haversian canal (μm).

osteocyte lacunar density was higher in the bone matrix where the bone porosity was lower, Fig. 6(c). As a comparison, the lacunar density remains more homogenous in the sample, which is more uniform in term of porosity, Fig. 6(d).

Correlations between bone porosity and osteocyte lacunar features

A quantitative evaluation of the relationships between osteocyte density and bone porosity was conducted on the sample displayed in Fig. 6(c). Lacunar density and lacunar descriptors were extracted from the seven sub-volumes displayed on Fig. 7. The linear regression analysis shows that several descriptors were strongly correlated with the *BV/TV* (Table 4 and Fig. 8). Among the correlations, lacunar number density, the three axes length of lacunae (*Lc.L1*, *Lc.L2*, and *Lc.L3*) and the anisotropy of the lacunae (*Lc.L1*/*Lc.L2* and *Lc.L1*/*Lc.L3*) were significantly correlated with the bone volume fraction (*BV/TV*). The volume and surface of the lacunae were not correlated to bone porosity.

Discussion

In this paper, after describing the imaging conditions with SR micro-CT and the segmentation of osteocyte lacunae, we proposed an automated method for extracting 3D shape descriptors on each osteocyte lacuna. We also introduced the 3D local lacunar density map to visualize the lacunar density variation within the bone sample. We reported the distribution and statistics on various morphological descriptors. Several strong correlations between osteocyte lacunar descriptors and bone porosities were also reported for the first time in 3D quantification.

The osteocytes are deeply enclosed in the compact bone matrix, making their quantification challenging with conventional imaging techniques. The proposed method has three main features: first it is based on a gold standard 3D imaging technique, second, it describes a robust segmentation of lacunae, and third, it rigorously defines and extracts 3D descriptors of lacunae. We want to emphasize that a well-controlled methodology, at each step of the process, is required to be able to draw reliable biological conclusions.

CT coupled to synchrotron radiation is considered as a gold standard for imaging the micro- and ultra-structure of the bone tissue [44]. It has recently been used to quantify the morphometry of osteocyte lacunae [27,28]. Using SR-micro CT to image the osteocyte lacuna has many advantages compared to other imaging techniques. First, it provides a 3D image with isotropic spatial resolution, allowing accurate and direct 3D measurements without any destruction of the sample. Most of the conventional studies on osteocyte lacunae were based on 2D imaging of thin section. However, the mechanical sectioning of the sample does not guarantee keeping the integrity of the structure. Nevertheless, with the rapid development of imaging techniques, the acquisition of three dimensional images of the osteocyte network has become possible The FIB/SEM technique has been demonstrated to deliver a very high resolution in depth and looks promising to quantify the osteocyte LCN at the order of tens of nanometers [13,21], but it still requires the physical destruction of the sample and the imaging process is quite time consuming. Second, SR-micro CT allows to image relatively large fields of view containing more than ten thousands of osteocyte lacunae. Therefore one can expect that the estimate of the average of the mean properties of lacunae to be improved compared to smaller populations. This can be assessed by the standard error of the mean (SEm) defined as the standard deviation divided by the square root of the number of analyzed lacunae. For example to give an order of the magnitude, in our study according to Tables 2 and 3, the SEm of the lacunar volume in A1 is 1.4, while it can be estimated to be 15.5 in the work of Sugawara. Comparatively, 3D confocal laser scanning microscopy (CLSM) has been successfully applied in several studies [15,16,23,33]. It has the advantages of high resolution and no ionizing radiation damage on the sample, but due to the limited penetration of light, up to now, the field of view within bone tissue has been confined to a maximum depth of 100–150 μm [45]. Third, the high X-ray flux available on synchrotron sources, which is several orders of magnitude higher than conventional X-ray, permits to acquire images with high signal to noise ratio (SNR) in relatively short scanning time. Although new generations of high resolution desktop CTs have also been demonstrated to analyze lacunae [16,23], they suffer from a lower SNR, making the segmentation of

Table 3
Osteocyte lacunar descriptors from 13 specimens "*" parameters reported with standard deviation and range [minimum, maximum].

Sample ID	Lc.V (μm^3)*	Lc.S (μm^2)*	Lc.L1 (μm)*	Lc.L2 (μm)*	Lc.L3 (μm)*
A1	446.2 ± 153.5	354.9 ± 94.4	20.1 ± 4.9	9.0 ± 2.1	5.0 ± 1.0
	[82.3,965.9]	[93.2,761.7]	[6.9,43.8]	[3.7,21.1]	[1.9,10.1]
A2	405.4 ± 147.7	330.5 ± 92.4	19.1 ± 4.8	8.7 ± 2.0	4.9 ± 1.0
	[82.3,902.8]	[97.9,734.0]	[7.5,40.5]	[3.8,18.2]	[1.0,9.9]
A3	427.0 ± 140.3	340.7 ± 86.5	19.8 ± 4.8	8.6 ± 1.9	5.1 ± 1.0
	[82.3,839.7]	[95.0,661.2]	[8.0,41.3]	[3.6,18.6]	[1.5,9.7]
A4	364.3 ± 147.1	311.5 ± 95.9	17.6 ± 4.7	9.1 ± 2.0	4.9 ± 1.2
	[82.3,954.9]	[93.1,724.7]	[6.4,40.9]	[3.3,19.0]	[1.4,10.8]
A5	410.0 ± 130.3	342.9 ± 85.7	18.9 ± 4.9	9.7 ± 2.0	4.9 ± 1.2
	[82.3,834.2]	[94.8,735.0	[6.4,45.2]	[3.6,19.1]	[1.5,10.4]
A6	353.3 ± 142.5	300.5 ± 90.3	18.4 ± 4.9	8.3 ± 1.9	4.6 ± 0.9
	[82.3,798.5]	[90.1,622.5]	[7.3,39.5]	[3.7,18.7]	[1.9,9.3]
A7	502.3 ± 151.2	386.5 ± 96.7	20.7 ± 5.6	9.5 ± 1.9	5.2 ± 1.0
	[82.3,902.8]	[96.8,738.7]	[8.0,40.3]	[3.7,18.0]	[0.7,11.1]
B1	386.2 ± 175.6	323.1 ± 112.1	18.4 ± 4.9	9.3 ± 2.3	4.4 ± 1.0
	[82.3,974.1]	[95.3,770.8]	[7.2,41.6]	[3.6,20.4]	[1.0,10.0]
B2	381.9 ± 138.1	312.7 ± 82.6	17.6 ± 4.0	9.1 ± 2.0	4.8 ± 1.0
	[82.3,902.8]	[96.4,688.5]	[7.4,37.2]	[3.5,20.4]	[1.6,10.3]
B3	430.5 ± 149.9	348.5 ± 92.4	19.1 ± 4.6	9.5 ± 2.0	4.8 ± 1.0
	[82.3,935.7]	[96.9,711.5]	[6.9,39.0]	[3.3,18.3]	[1.4,10.5]
B4	409.7 ± 137.4	349.0 ± 93.4	19.2 ± 4.9	10.0 ± 2.1	4.6 ± 1.1
	[82.3,974.1]	[93.8,800.8]	[7.0,42.7]	[3.9,20.5]	[1.5,10.7]
B5	377.4 ± 129.7	320.1 ± 86.1	17.8 ± 4.4	9.6 ± 2.0	4.8 ± 1.1
	[82.3,880.8]	[93.2,742.0]	[6.7,46.5]	[3.9,19.2]	[1.0,11.1]
B6	402.6 ± 146.5	334.1 ± 91.2	18.8 ± 4.5	9.5 ± 2.1	4.5 ± 0.9
	[82.3,809.5]	[95.9,680.3]	[7.6,36.6]	[4.0,18.4]	[0.9,10.1]
A	417.6 ± 152.4	339.7 ± 95.8	19.3 ± 5.1	9.0 ± 2.0	5.0 ± 1.1
	[82.3,965.9]	[90.1,761.7]	[6.4,45.2]	[3.3,21.1]	[0.7,11.1]
B	398.4 ± 145.2	331.4 ± 92.5	18.5 ± 4.6	9.5 ± 2.1	4.7 ± 1.0
	[82.3,974.1]	[93.2,800.8]	[6.7,46.5]	[3.3,20.5]	[0.9,11.1]
All	409.5 ± 149.7	336.2 ± 94.5	18.9 ± 4.9	9.2 ± 2.1	4.8 ± 1.1
	[82.3,974.1]	[90.1,800.8]	[6.4,46.5]	[3.3,21.1]	[0.7,11.1]

Sample ID	Lc.L1/Lc.L2*	Lc.L1/Lc.L3*	Lc.SMI*	$Lc.Dist_{50}$ (μm)	$Lc.Dist_{95}$ (μm)	Ratio (τ)
A1	2.4 ± 0.8	4.2 ± 1.2	3.3 ± 0.2	14.0	28.0	94.8% ± 5.0%
	[2.8,7.2]	[1.3,11.3]	[2.4,4.0]			
A2	2.3 ± 0.8	4.1 ± 1.3	3.4 ± 0.2	14.0	26.6	94.5% ± 5.2%
	[2.8,7.1]	[1.3,14.9]	[2.3,4.3]			
A3	2.4 ± 0.8	4.1 ± 1.2	3.4 ± 0.2	14.0	28.0	95.3% ± 4.8%
	[1.0,5.0]	[1.3,12.3]	[2.2,4.1]			
A4	2.0 ± 0.7	3.8 ± 1.5	3.3 ± 0.3	14.0	29.4	88.1% ± 8.6%
	[2.8,6.8]	[1.2,27.5]	[2.3,4.4]			
A5	2.1 ± 0.8	4.1 ± 1.6	3.3 ± 0.3	12.6	23.8	89.1% ± 7.6%
	[2.8,6.9]	[1.1,12.6]	[1.9,4.3]			
A6	2.3 ± 0.8	4.1 ± 1.3	3.4 ± 0.2	14.0	26.6	94.6% ± 4.8%
	[2.8,7.1]	[1.4,14.3]	[2.3,4.4]			
A7	2.3 ± 0.8	4.1 ± 1.4	3.3 ± 0.2	12.6	23.8	94.8% ± 4.9%
	[2.8,7.5]	[1.2,34.9]	[2.3,4.4]			
B1	2.1 ± 0.7	4.3 ± 1.3	3.3 ± 0.3	16.8	33.6	95.0% ± 5.4%
	[2.8,6.5]	[1.3,16.7]	[2.2,4.0]			
B2	2.1 ± 0.7	3.8 ± 1.2	3.4 ± 0.2	14.0	28.0	94.5% ± 5.3%
	[2.8,7.1]	[1.3,12.8]	[2.4,4.1]			
B3	2.1 ± 0.7	4.2 ± 1.3	3.3 ± 0.2	14.0	28.0	94.5% ± 5.5%
	[2.8,7.2]	[1.4,15.5]	[2.4,4.1]			
B4	2.0 ± 0.7	4.5 ± 1.6	3.2 ± 0.3	14.0	26.6	90.1% ± 7.4%
	[2.8,6.8]	[1.2,15.5]	[2.0,4.2]			
B5	1.9 ± 0.7	4.0 ± 1.5	3.3 ± 0.3	14.0	26.6	90.5% ± 7.4%
	[2.8,6.9]	[1.2,18.8]	[2.1,4.3]			
B6	2.1 ± 0.7	4.3 ± 1.3	3.2 ± 0.2	14.0	28.0	95.6% ± 4.3%
	[2.8,7.1]	[1.2,21.1]	[2.2,4.1]			
A	2.3 ± 0.8	4.1 ± 1.4	3.3 ± 0.2	13.5 ± 0.7	26.3 ± 2.1	92.9% ± 6.7%
	[1.0,7.5]	[1.1,34.9]	[1.9,4.4]			
B	2.0 ± 0.7	4.2 ± 1.4	3.3 ± 0.3	14.3 ± 1.1	28.0 ± 2.6	93.2% ± 6.5%
	[2.8,7.2]	[1.2,21.1]	[2.0,4.3]			
All	2.2 ± 0.8	4.1 ± 1.4	3.3 ± 0.3	13.8 ± 1.0	27.0 ± 2.5	93.1% ± 6.6%
	[1.0,7.5]	[1.1,34.9]	[1.9,4.4]			

Lc.V—lacunar volume (μm^3).
Lc.S—lacunar surface area (μm^2).
Lc.L1, Lc.L2 and Lc.L3—length, width and depth of lacuna (μm).
Lc.L1/Lc.L2 and Lc.L1/Lc.L3—anisotropy of lacuna.
Lc. SMI—structural model index of lacuna.
$Lc.Dist_{50}$—average distance of 50% of bone matrix to the nearest lacuna (μm).
$Lc.Dist_{95}$—average distance of 95% of bone matrix to the nearest lacuna (μm).
Ratio (τ)—volume ratio of lacuna to fitting ellipsoid (%).

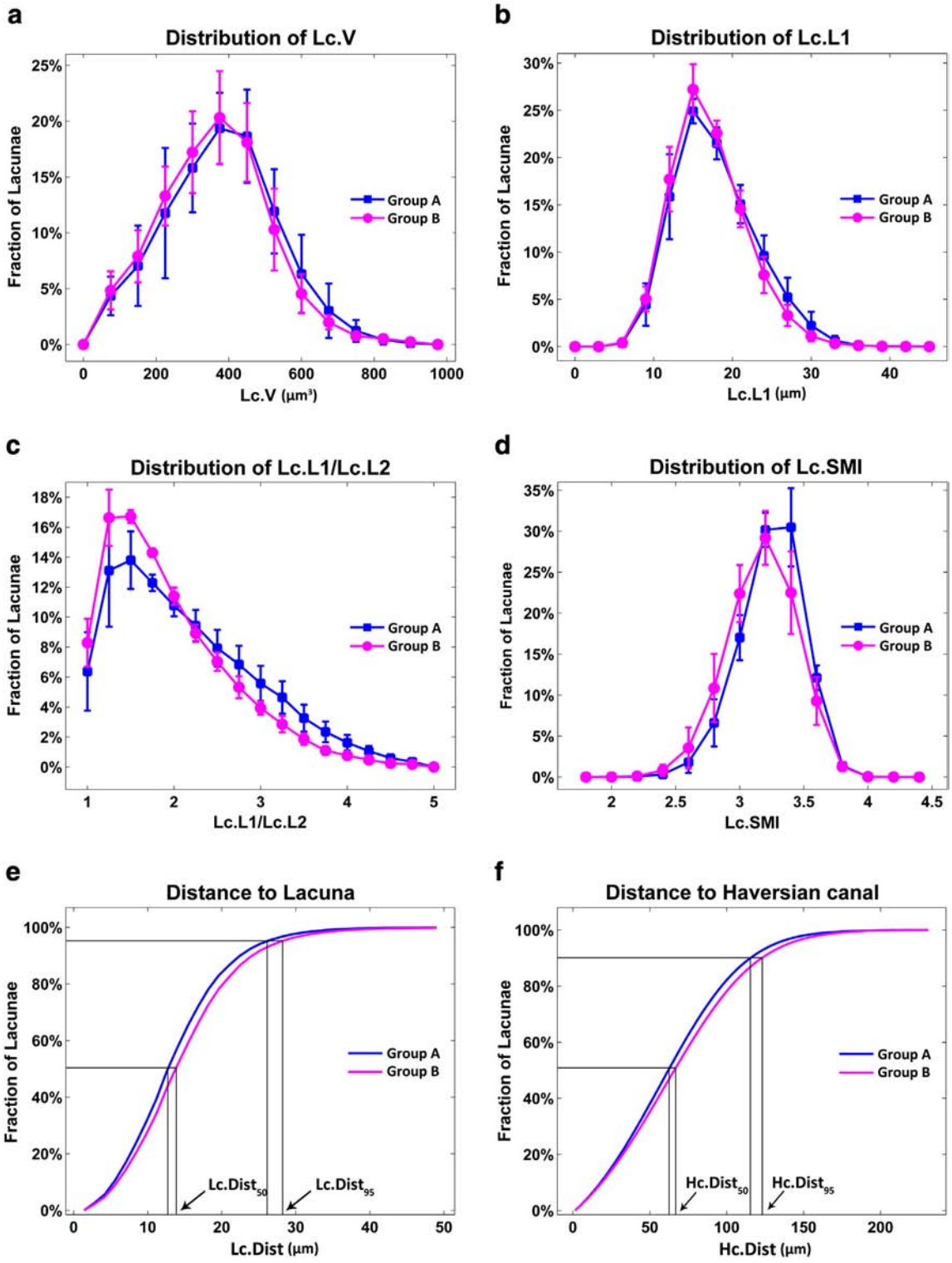

Fig. 5. Lacunar descriptor distributions of group A (blue curve) and group B (pink curve). (a)–(d): Average distribution (line) and standard deviation (bars) of lacunar volume (a), main axis length (b), anisotropy (c) and structure model index (d). (e)–(f): Average distance distribution from bone matrix to osteocyte lacunae (e) and from bone matrix to Haversian canals (f). (For interpretation of the references to color in this figure legend, the reader is referred to the web version of this article.)

small objects such as lacunae more difficult. Apart from the advantage mentioned above, SR micro-CT techniques can also reach nanometric resolution [22,46,47] to image lacunae and canaliculi but this was out of the scope of this work.

In this work, we detailed a robust automatic method based on hysteresis thresholding followed by a step of artifact elimination to segment the osteocyte lacunae from the SR micro-CT images. The need for an automatic method is clear when considering that the 3D images enclose thousands of lacunae. With a voxel size of 1.4 μm, the osteocyte lacunae appear as quite small structures. By applying the hysteresis thresholding on the reconstructed image, the osteocyte lacunae with various grey values could be well preserved. By taking into account the morphology of the osteocyte lacunae, artifacts, such as noise, ring artifacts, and irregular shaped objects were well eliminated, thus the

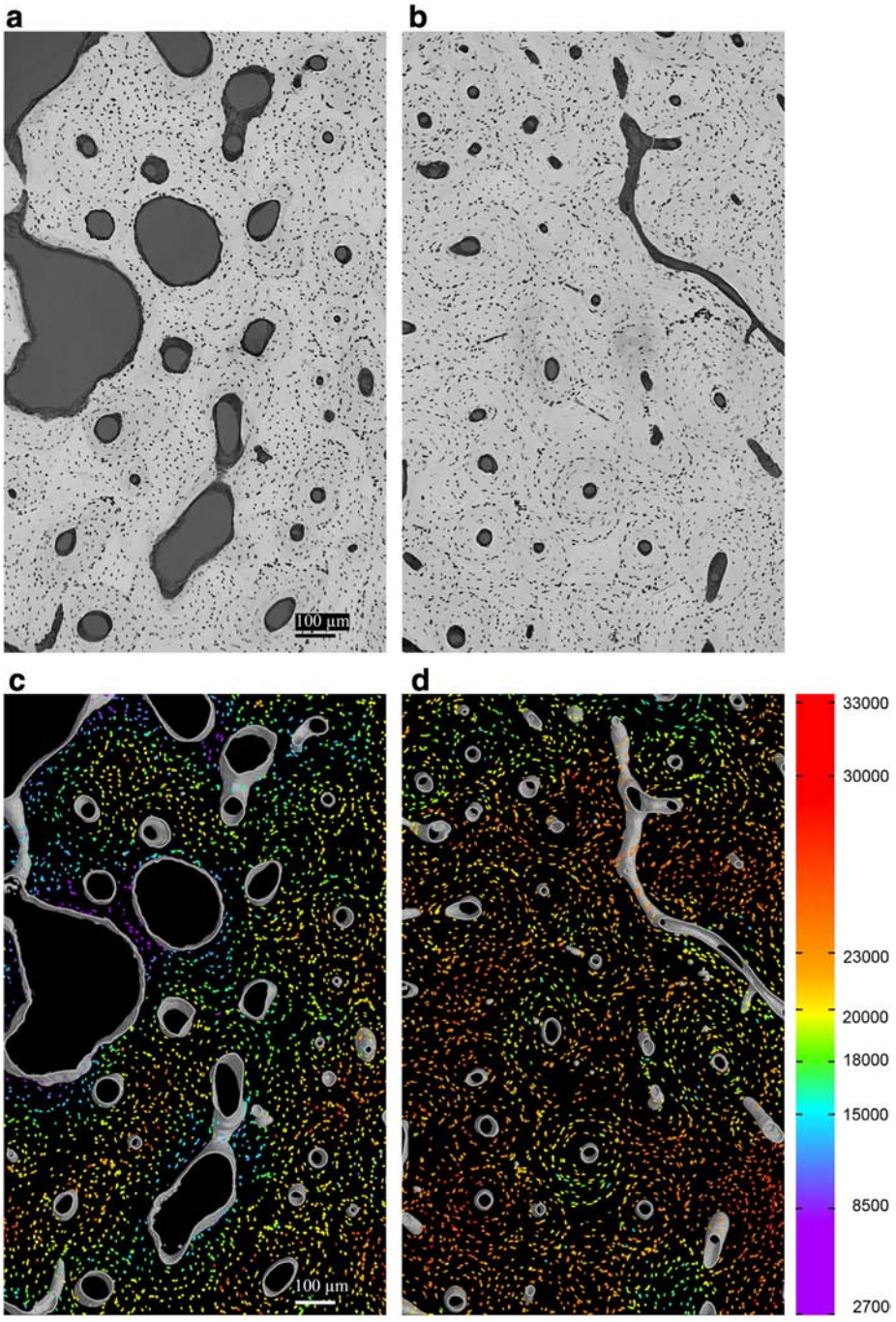

Fig. 6. (a) and (b) minimum of projection of 61 slides of the reconstruction images. The bone porosity of (a) (sample A3) varies a lot, while in comparison, the bone porosity of (b) (sample B2) remains quite homogeneous. (c) and (d) are the corresponding 3D lacunar density maps (N.Lc(r)/BV(r)) (r = 140 μm) of (a) and (b). The unit of the colored legend bar is #/mm^3. The cold color (blue) represents a low lacunar density, and warm color (red) represents a high lacunar density. (For interpretation of the references to color in this figure legend, the reader is referred to the web version of this article.)

method is robust to noise. This automatic method was compared to a semi-manually segmented image. The quantitative results indicate reliable results since the Dice index was 94.6% and the relative errors between the descriptors calculated on the segmented and on the reference image differed by less than 2%. It would be desirable to validate the method on more reference images but the manual segmentation is not a trivial task since it requires a lot of user interaction. The reference image segmented here contained 357 lacunae, which is already a large number compared to most manual studies (for instance in [30], there were only 75 lacunae per sections). Thus, the manual segmentation of more images would be a hugely time-consuming task and subject to bias from human fatigue and subjectivity. Our method also excluded those fragmented lacunae on the border of the 3D image, which might not be done in previous studies [27,28]. The removal of these fragmented lacunae is important, since they can influence the lacunae descriptors distribution on the whole population. Actually, the segmentation is a crucial step when quantitative parameters are expected since an incorrect segmentation may bias the results. To the best of our knowledge, no other segmentation method of osteocyte lacunae has so far been evaluated. In previous works based on 2D imaging, the segmentation of the osteocyte lacunae was mostly performed interactively by using 2D commercial image processing software [15,16,23,33,45]. In other works based on 3D imaging, simple thresholding was generally used. For instance, in Carter [28], lacunae were extracted from global

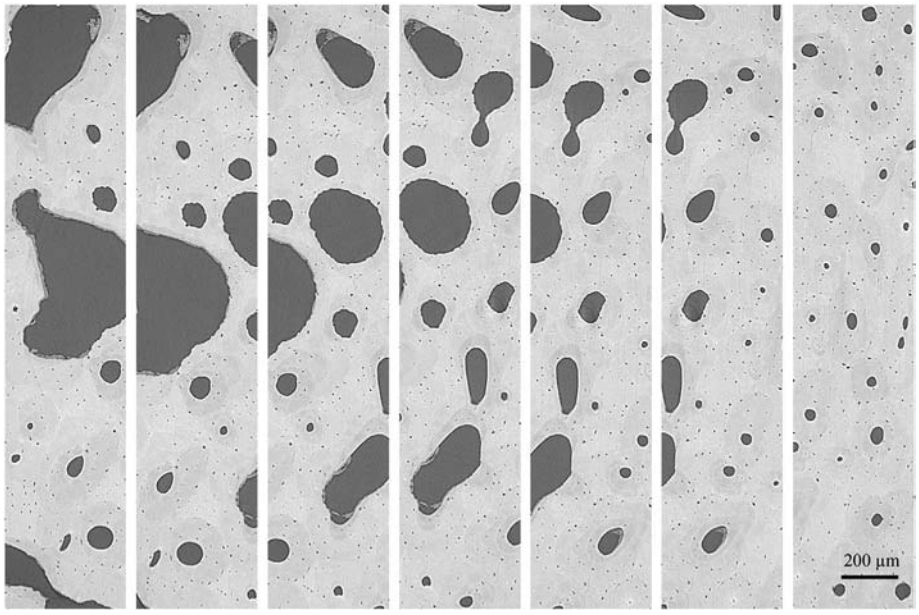

Fig. 7. A series of regions with different tissue porosities from a single sample.((a)–(g): BV/TV ranging from 67% to 97%).

thresholding, followed by the elimination of noise based only on the volume of each object, but the authors did not report validation results.

At the tissue level, on average, 12,791 ± 2531 lacunae were successfully segmented from a tissue region of 1.4 mm × 1.4 mm × 0.35 mm, corresponding to a density of 20,573 ± 2850 lacunae per mm^3. This finding is in range of previous 3D reports on the number of lacunae per bone volume both at high (580 nm) [16] and lower (1.4 μm) [28] spatial resolution. We also reported the distances reflecting the distribution of Haversian canals. To the best of our knowledge, it is the first time that these values are reported in human. The results are similar to that found by Shahar in dogs and horses by using 2D microscopic images [48]. These parameters, for which estimation is more reliable in 3D, may be important indicators of how efficiently blood can support the nutrient for the bone tissue.

We calculated a number of direct 3D lacunar descriptors. In general, many studies highlighted the important role of the osteocyte in mechanotransduction and in controlling bone remodeling. However, relatively few descriptive parameters on the size, shape, density and spatial organization of the osteocyte lacunae are available in 3D. It is known that these morphological characteristics impact the biomechanical parameters. For instance, it was shown that the mechanical environment of the stress-sensitive osteocyte varies with the geometry of the osteocyte lacuna [33]. More recently the shape of the osteocyte was found to have a direct impact on elasticity and mechanosensing [10]. In addition, most theoretical biomechanical models require assumptions about the density, shape and size of lacunae. In a simulation study, Mullins et al. showed the impact of varying lacunar porosity on the macroscopic properties of cortical bone [11]. Thus the descriptive parameters we provide can further be used as realistic input to biomechanical models.

In addition, this study provides an analysis of the spatial organization of lacunae within bone matrix that could have some interpretation in terms of the bone mineral homeostasis process. While the role of osteocytes in this process is still a subject of debate [49], a recent work suggests that osteocytes contribute directly to the calcium homeostasis by removing their surrounding mineral matrix [9]. We found that although the total lacunar volume is smaller than that of the Haversian canals, their spatial distribution put them closer to the mineral matrix than the Haversian canal. This spatial organization might be important for the interplay of the cell network and the bone matrix.

Three dimensional measurements are more accurate than those derived from 2D images, generally based on ideal geometric assumption. For example, Mullender estimated the 3D lacunar density from 2D lacunar density based on the spherical shape assumption [30]. By simulating a 2D image from our 3D binary lacunar image by stacking 4 consecutive slices (equivalent slice thickness 5.6 μm), we used the same method to extrapolate 2D density measurements in 3D. We obtained a 2D density of about 380 mm^{-2}, and an extrapolated 3D density of 30,600 mm^{-3}, while the actual 3D lacunar density (N.Lc/BV) was 20,471 mm^{-3}. This illustrates the bias than can be introduced by an incorrect model assumption. In addition, the lower lacunar 3D density values obtained in Mullender's work can be related to the fact that when counting manually in 2D, only the large lacunae may be kept, thus underestimating the density.

In this study, the average and standard deviation of the lacunar volume was 409.5 ± 149.7 $μm^3$, and its surface was 336.2 ± 94.5 $μm^2$. The lacunar volume measured in the current study is consistent with previously reported values. For instance, Carter [28] measured lacunae volumes between 378 and 409 $μm^3$ at different anatomic locations within a healthy young male femoral shaft from SR micro-CT images. McCreadie also found a similar average value (476 $μm^3$) on 609 lacunae from 28 women femoral head using 3D CLSM image [33]. Regarding the lacunar surface in 3D, this parameter was less often reported. Van

Table 4
Regression statistics on the parameters calculated on the seven subvolumes displayed in Fig. 7 "*" indicate parameters reported with $p < 0.05$.

Regression statistics	BV/TV	R^2	Slope	Intercept
N.Lc/BV	Positive	0.85*	10,461*	10,345*
Lc.L1	Negative	0.69*	−4.24*	23.26*
Lc.L2	Positive	0.95*	1.05*	7.81*
Lc.L3	Positive	0.95*	0.95*	4.28*
Lc.L1/Lc.L2	Negative	0.78*	−0.77*	3.02*
Lc.L1/Lc.L3	Negative	0.93*	−1.59*	5.38*
Lc.SMI	Positive	0.95*	0.15*	3.24*
Lc.V	Positive	0.12	25.13	410.43*
Lc.S	Negative	0.05	−10.37	351.38*

N.Lc/BV—lacunar number density (mm^{-3}).
Lc.L1, Lc.L2 and Lc.L3—length, width and depth of lacuna (μm).
Lc.L1/Lc.L2 and Lc.L1/Lc.L3—anisotropy of lacuna.
Lc. SMI—structural model index of lacuna.
Lc.V—lacunar volume ($μm^3$).
Lc.S—lacunar surface area ($μm^2$).

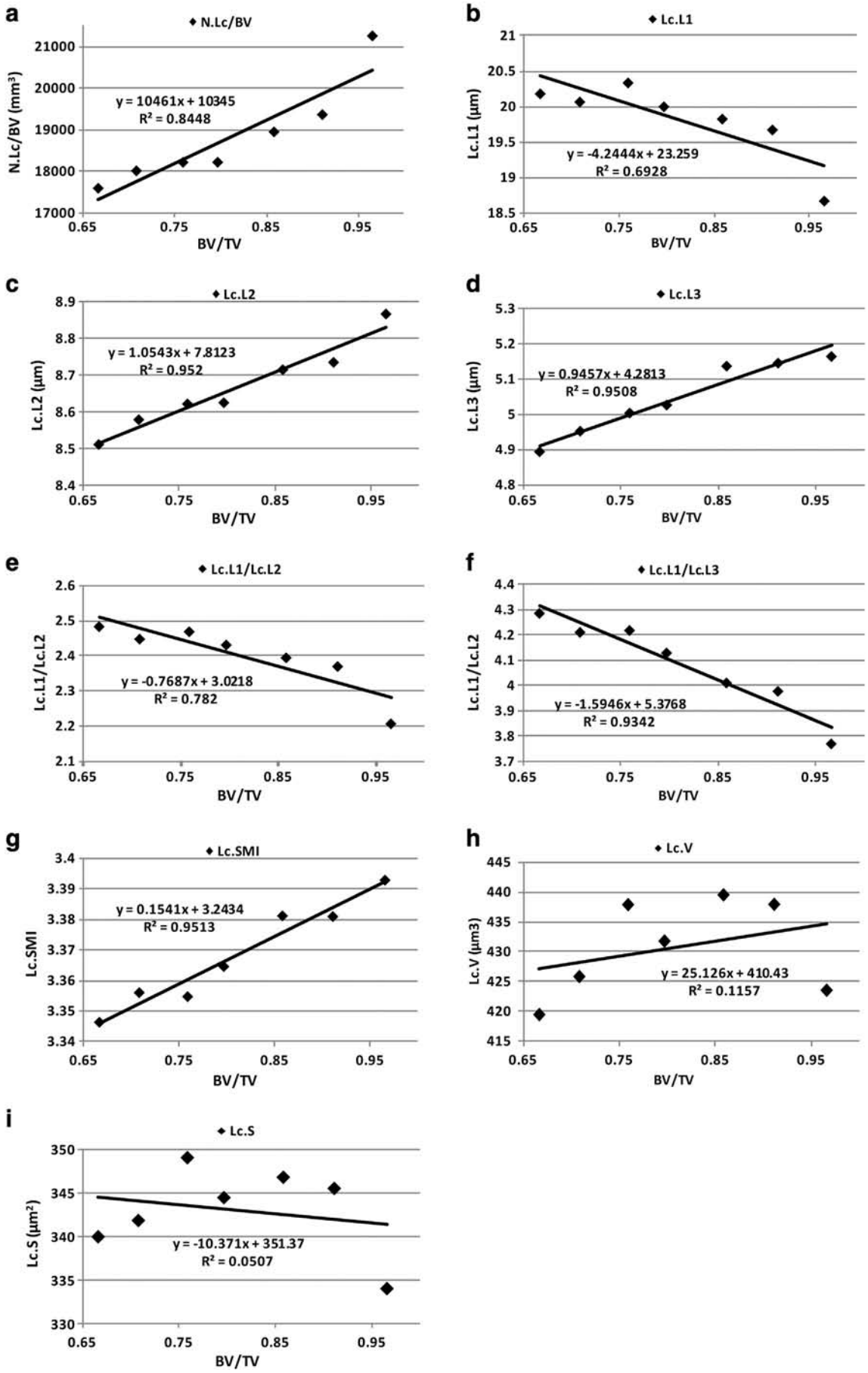

Fig. 8. Correlation of bone porosity with osteocyte lacunar density (a), axes lengths (b)–(d), anisotropy (e)–(f), SMI (g), volume(h) and surface area(i).

Hove [16], found lacunar surfaces between 94.6 ± 2.8 μm^2 to 211.9 ± 14.4 μm^2 from desktop nano-CT images in three human proximal tibial bone samples, from osteopenic, osteoarthritic and osteopetrotic patients. Compared to previous studies, we may note that differences existed in donor age and sex, anatomic location of the measurements and the imaging modality between the current and previous studies.

We found that the axis lengths were on average 18.9 ± 4.9 μm, 9.2 ± 2.1 μm and 4.8 ± 1.1 μm. The ratio of the three axis lengths is quite close to 4:2:1. These values are quite in agreement with the result reported by Van Hove [16]. Defining the anisotropy as the ratio of minimum to maximum dimensions, McCreadie [33] found the similar degrees of anisotropy (0.271 and 0.279) of osteocyte in female femoral fracture and controlled samples, which is quite similar to the value we reported (0.254). Our findings also support the result of Vatsa [23] who found a stretched structure of osteocytes in fibular bone, where osteocyte were aligned along the direction of loading, whereas osteocytes in calvarial bone, which do not bear a mechanical loading, had a more spherical shape with ratio of 2.1:1.3:1, and were not aligned to a particular direction. Carter [28] did not directly report the axis lengths but three eigenvalues (EV) supposed to be the square of half-length of each main axis. However, the corresponding half-length values derived by using this relationship seem to give underestimated axis lengths compared to the literature. Besides, Carter also reported a degree of equancy (1 − EV3/EV1), a degree of elongation (1 − EV2/EV1) and a degree of flatness (1 − EV3/EV2) to describe the shape of lacunae. By using the same definition, we found a similar average degree of elongation (0.760) but flatter lacunae (0.725).

Besides the usual parameters, such as volume, surface, axis lengths and anisotropy, we also calculated other descriptors: the 3D Euler number depicts the lacunar topology, the SMI characterizes the plate-rod like nature of the lacuna, and the distance map describes the distance of bone matrix to the nearest osteocyte lacunae. In theory the Euler number of an ideal lacuna is 1. However, in practice, due to noise and artifacts in image acquisition, we observed different values (for instance for irregularly-shaped artifact which are not lacunae). Thus the 3D Euler number was mainly used to eliminate this kind of noise. The Lc.SMI was on average 3.3 ± 0.3 showing a structure between a cylinder and a sphere [38]. The average distance of bone matrix to the nearest osteocyte lacunae is larger than the value found by Kerschnitzki [37]. He reported that 80% of the bone matrix is within a distance of 10 μm to the adjacent osteocyte in sheep. The difference could be explained by the different species used in the experiment. The reported Lc.Dist$_{50}$ and Lc.Dist$_{95}$ might be a well-suited descriptor which summarizes not just the amount of pores, but also their spatial distribution which is of importance in term of calcium homeostasis and its microenvironment remodeling [9]. These descriptors are generally not reported since they are not available in standard commercial software.

Furthermore, our method provides the statistical distribution of each descriptor (see Fig. 5). The distribution of the lacunar volume did not appear to be bimodal contrary to what was found by Hannah [27]. Two potential reasons might explain that. First, our study included the lacunae from both osteon and interstitial tissue in female subjects, while Hannah's one restricted to osteons on a younger male subject. Second, in our study, the truncated lacunae at the periphery of the volume were excluded. Keeping the truncated lacunae could contribute in a second artifactual peak in the volume distribution.

Proper 3D display is a powerful method for exploratory research. By introducing 3D renderings of the local density of osteocyte lacunae (*N.Lc(r)/BV(r)*) (Fig. 6), it was easy and intuitive to find the possible relationship between osteocyte lacunar density and bone porosity even before doing any statistical studies. Fig. 6(c) reveals that lacunar density can be quite low (2700/mm^3) close to very porous region and can rise up to 30,000/mm^3 around dense bone matrix regions. However, such large density variations were not observed in more homogenous bone regions (Fig. 6(d)).

The quantitative study on different bone porosity regions showed that lacunar density (*N.Lc/BV*) was strongly correlated ($R^2 = 0.845$, $p = 0.0034$) with the change of bone porosity. The linear regression showed that with every 1% increase of bone porosity, the lacunar density decreases of 104.61/mm^3. Such negative correlation between bone porosity and lacunar density is in agreement with the work of Power [50] conducted in 2D using light microscopy. His work was based on several regions across different sites of bone including superior, inferior, anterior and posterior regions on female femoral neck across biopsy (fractured) and post-mortem (controlled) samples. A strong correlation between lacunar density and BV/TV bone porosity, was reported by Vashishth et al. [51,52], who conducted the study with a series of different aged subjects using light microscopy. Our results, although limited, support the hypothesis that the lacunar density determines the bone volume fraction. More interestingly, we also found that several other lacunar descriptors correlated with *BV/TV*. The lacunar anisotropies (*Lc.L1/Lc.L2* and *Lc.L1/Lc.L3*) were significantly larger in a more porous bone region. The increase of anisotropy was mainly due to the increase in the length of lacunae in the more porous bone region, as the width and depth were slightly decreased in contrast. The correlation between BV/TV and Lc.SMI also confirm that the lacunae were on average more rod-like structures than sphere-like in regions of higher bone porosity. Information on lacunar shape might be important since they might reflect the mechanical properties of the cortical bone [53].

There are some limitations of this study. First, although thirteen samples were analyzed, we acknowledge that they arise from only two donors thus limiting the generality of the results. Also, the correlation study between the bone porosity and lacunar density was based on a single sample but with diverse porosities. However, our results are quite consistent with previous work conducted in 2D [50–52]. Since our results were 3D descriptors calculated from SR CT images on a large number of cells, they can be more reliable. The lacunar characteristics as well as their correlations to porosity need to be further studied on more samples of different individuals and at different anatomical locations. Second, the voxel size of 1.4 μm could be limited to image very small lacunae, but it was our choice to provide a large field of view that allows the analysis of a large population of cells. Third, the imaging technique used in this study can only detect the hard tissue. Therefore, it was impossible to image and quantify the osteocytes inside the lacunae. We believe that reporting descriptive data on the osteocyte lacunae contributes to the field since there are relatively few 3D data available in the literature. But it is difficult to give an extensive interpretation of the results since we have relatively few information on the donors. In further study, we plan to compare osteocyte lacunae in samples from healthy donors and diseased patients.

To summarize, in this study, we presented an automatic and well controlled methodology for quantitative analysis on a large population (more than 150,000) of osteocyte lacunae. The 3D images were acquired through a SR micro-CT system, which is currently considered a gold standard for the observation of the osteocyte lacunae. We delivered an automated method to perform the segmentation, parameters extraction and statistics. Considerations, such as artifact elimination and partial lacunae removal, were carefully handled in the process. Since the calculation on each parameter was performed directly in 3D, unbiased results can be delivered compared to the previous results derived from ideal model assumptions. The results were compared with a reference image, and were proved to be reliable. We developed our own software, including novel parameters regarding the shape of lacunae. By introducing the 3D local lacunar density map, it was possible to visualize the lacunar density variation over large field of view. Further, by using these tools, we found several significant relationships between the osteocyte lacunar descriptors and bone porosity at the same local region in 3D. We believe that using such method will boost the efficiency on the investigation of osteocyte lacunar shape analysis over a large number of specimens. Therefore, it will help the researchers to investigate the bone related

problems associated with the reliable statistical data at cell level more directly, effectively and quantitatively.

Acknowledgment

The authors acknowledge the support of the ESRF for providing beamtime on beamline ID19 for synchrotron micro-CT imaging in the context of the Long term Project (LTP) MD431 and the help of the ID19 group during data acquisition. This work was done within the framework of the French GdR STic Santé (GdR 2643) and of the LabEx PRIMES (ANR-11-LABX-0063) of the Université de Lyon within the Program "Investissements d'Avenir" (ANR-11-IDEX-0007) operated by the French National Research Agency.

References

[1] Ciarelli MJ, Goldstein SA, Kuhn JL, Cody DD, Brown MB. Evaluation of orthogonal mechanical properties and density of human trabecular bone from the major metaphyseal regions with materials testing and computed tomography. J Orthop Res 1991;9:674–82.
[2] Seeman E, Delmas PD. Bone quality—the material and structural basis of bone strength and fragility. N Engl J Med 2006;354:2250–61.
[3] Bonewald LF. The amazing osteocyte. J Bone Miner Res 2011;26:229–38.
[4] Bonucci E. The osteocyte: the underestimated conductor of the bone orchestra. Rend Lincei 2009;20:237–54.
[5] Bonewald LF, Johnson ML. Osteocytes, mechanosensing and Wnt signaling. Bone 2008;42:606–15.
[6] Bonewald LF. Mechanosensation and transduction in osteocytes. Bonekey Osteovision 2006;3:7–15.
[7] Burger EH, Klein-Nulend J. Mechanotransduction in bone—role of the lacuno-canalicular network. FASEB J 1999(13 Suppl.):S101–12.
[8] Westbroek I, De Rooij KE, Nijweide PJ. Osteocyte-specific monoclonal antibody MAb OB7.3 is directed against Phex protein. J Bone Miner Res 2002;17:845–53.
[9] Qing H, Ardeshirpour L, Pajevic PD, Dusevich V, Jähn K, Kato S, et al. Demonstration of osteocytic perilacunar/canalicular remodeling in mice during lactation. J Bone Miner Res 2012;27:1018–29.
[10] Bacabac RG, Mizuno D, Schmidt CF, MacKintosh FC, Van Loon JJWA, Klein-Nulend J, et al. Round versus flat: bone cell morphology, elasticity, and mechanosensing. J Biomech 2008;41:1590–8.
[11] Mullins LP, McGarry JP, Bruzzi MS, McHugh PE. Micromechanical modelling of cortical bone. Comput Methods Biomech Biomed Engin 2007;10:159–69.
[12] Currey JD. The many adaptations of bone. J Biomech 2003;36:1487–95.
[13] Schneider P, Meier M, Wepf R, Müller R. Towards quantitative 3D imaging of the osteocyte lacuno-canalicular network. Bone 2010;47:848–58.
[14] Hirose S, Li M, Kojima T, de Freitas PHL, Ubaidus S, Oda K, et al. A histological assessment on the distribution of the osteocytic lacunar canalicular system using silver staining. J Bone Miner Metab 2007;25:374–82.
[15] Sugawara Y, Kamioka H, Honjo T, Tezuka K, Takano-Yamamoto T. Three-dimensional reconstruction of chick calvarial osteocytes and their cell processes using confocal microscopy. Bone 2005;36:877–83.
[16] Van Hove RP, Nolte PA, Vatsa A, Semeins CM, Salmon PL, Smit TH, et al. Osteocyte morphology in human tibiae of different bone pathologies with different bone mineral density—is there a role for mechanosensing? Bone 2009;45:321–9.
[17] Boyde A, Jones SJ. Scanning electron microscopy of bone: instrument, specimen, and issues. Microsc Res Tech 1996;33:92–120.
[18] Okada S, Yoshida S, Ashrafi SH, Schraufnagel DE. The canalicular structure of compact bone in the rat at different ages. Microsc Microanal 2002;8:104–15.
[19] You LD, Weinbaum S, Cowin SC, Schaffler MB. Ultrastructure of the osteocyte process and its pericellular matrix. Anat Rec A Discov Mol Cell Evol Biol 2004;278:505–13.
[20] Rubin MA, Rubin J, Jasiuk I. SEM and TEM study of the hierarchical structure of C57BL/6J and C3H/HeJ mice trabecular bone. Bone 2004;35:11–20.
[21] Schneider P, Meier M, Wepf R, Müller R. Serial FIB/SEM imaging for quantitative 3D assessment of the osteocyte lacuno-canalicular network. Bone 2011;49:304–11.
[22] Dierolf M, Menzel A, Thibault P, Schneider P, Kewish CM, Wepf R, et al. Ptychographic X-ray computed tomography at the nanoscale. Nature 2010;467:436–9.
[23] Vatsa A, Breuls RG, Semeins CM, Salmon PL, Smit TH, Klein-Nulend J. Osteocyte morphology in fibula and calvaria—is there a role for mechanosensing? Bone 2008;43:452–8.
[24] Salomé M, Peyrin F, Cloetens P, Odet C, Laval-Jeantet AM, Baruchel J, et al. A synchrotron radiation microtomography system for the analysis of trabecular bone samples. Med Phys 1999;26:2194–204.
[25] Peyrin F, Salome M, Cloetens P, Laval-Jeantet AM, Ritman E, Rüegsegger P. Micro-CT examinations of trabecular bone samples at different resolutions: 14, 7 and 2 micron level. Technol Health Care 1998;6:391–401.
[26] Hengsberger S, Enstroem J, Peyrin F, Zysset P. How is the indentation modulus of bone tissue related to its macroscopic elastic response? A validation study. J Biomech 2003;36:1503–9.
[27] Hannah KM, Thomas CDL, Clement JG, De Carlo F, Peele AG. Bimodal distribution of osteocyte lacunar size in the human femoral cortex as revealed by micro-CT. Bone 2010;47:866–71.
[28] Carter Y, Thomas CDL, Clement JG, Peele AG, Hannah K, Cooper DML. Variation in osteocyte lacunar morphology and density in the human femur—a synchrotron radiation micro-CT study. Bone 2012;52:126–32.
[29] Marotti G. Osteocyte orientation in human lamellar bone and its relevance to the morphometry of periosteocytic lacunae. Metab Bone Dis Relat Res 1979;1:325–33.
[30] Mullender MG, van der Meer DD, Huiskes R, Lips P. Osteocyte density changes in aging and osteoporosis. Bone 1996;18:109–13.
[31] Skedros JG, Grunander TR, Hamrick MW. Spatial distribution of osteocyte lacunae in equine radii and third metacarpals: considerations for cellular communication, microdamage detection and metabolism. Cells Tissues Organs 2005;180:215–36 (Print).
[32] Beno T, Yoon Y-J, Cowin SC, Fritton SP. Estimation of bone permeability using accurate microstructural measurements. J Biomech 2006;39:2378–87.
[33] McCreadie BR, Hollister SJ, Schaffler MB, Goldstein S a. Osteocyte lacuna size and shape in women with and without osteoporotic fracture. J Biomech 2004;37:563–72.
[34] Granke M, Grimal Q, Saïed A, Nauleau P, Peyrin F, Laugier P. Change in porosity is the major determinant of the variation of cortical bone elasticity at the millimeter scale in aged women. Bone 2011;49:1020–6.
[35] Canny J. A computational approach to edge detection. IEEE Trans Pattern Anal Mach Intell 1986;PAMI-8:679–98.
[36] Hoshen J, Kopelman R. Percolation and cluster distribution I. Cluster multiple labeling technique and critical concentration algorithm. Phys Rev B 1976;14:3438.
[37] Kerschnitzki M, Kollmannsberger P, Burghammer M, Duda GN, Weinkamer R, Wagermaier W, et al. Architecture of the osteocyte network correlates with bone material quality. J Bone Miner Res 2013;28:1837–45.
[38] Hildebrand T, Rüegsegger P. Quantification of bone microarchitecture with the structure model index. Comput Methods Biomech Biomed Engin 1997;1:15–23.
[39] Ohser J, Schladitz K. 3D images of materials structures: processing and analysis. Wiley; 2009.
[40] Ohser J, Nagel W, Schladitz K. The Euler number of discretized sets—on the choice of adjacency in homogeneous lattices. In: Mecke K, Stoyan D, editors. Morphology of condensed matter. Berlin Heidelberg: Springer; 2002. p. 275–98.
[41] Ohser J, Nagel W, Schladitz K. Miles formulae for Boolean models observed on lattices. Image Anal Stereol 2009;28:77–92.
[42] Schladitz K, Ohser J, Nagel W. Measuring intrinsic volumes in digital 3D images. In: Kuba A, Nyúl LG, Palágyi K, editors. Discrete geometry for computer imagery. Berlin Heidelberg: Springer; 2006. p. 247–58.
[43] Dice LR. Measures of the amount of ecologic association between species. Ecology 1945;26:297.
[44] Müller R. Hierarchical microimaging of bone structure and function. Nat Rev Rheumatol 2009;5:373–81.
[45] Jones CW, Smolinski D, Keogh A, Kirk TB, Zheng MH. Confocal laser scanning microscopy in orthopaedic research. Prog Histochem Cytochem 2005;40:1–71.
[46] Pacureanu A, Langer M, Boller E, Tafforeau P, Peyrin F. Nanoscale imaging of the bone cell network with synchrotron X-ray tomography: optimization of acquisition setup. Med Phys 2012;39:2229–38.
[47] Langer M, Pacureanu A, Suhonen H, Grimal Q, Cloetens P, Peyrin F. X-ray phase nanotomography resolves the 3D human bone ultrastructure. PLoS One 2012;7:e35691.
[48] Shahar R, Lukas C, Papo S, Dunlop JWC, Weinkamer R. Characterization of the spatial arrangement of secondary osteons in the diaphysis of equine and canine long bones. Anat Rec (Hoboken) 2011;294:1093–102.
[49] Teti A, Zallone A. Do osteocytes contribute to bone mineral homeostasis? Osteocytic osteolysis revisited. Bone 2009;44:11–6.
[50] Power J, Noble BS, Loveridge N, Bell KL, Rushton N, Reeve J. Osteocyte lacunar occupancy in the femoral neck cortex: an association with cortical remodeling in hip fracture cases and controls. Calcif Tissue Int 2001;69:13–9.
[51] Vashishth D, Gibson G, Kimura J, Schaffler MB, Fyhrie DP. Determination of bone volume by osteocyte population. Anat Rec 2002;267:292–5.
[52] Vashishth D, Verborgt O, Divine G, Schaffler MB, Fyhrie DP. Decline in osteocyte lacunar density in human cortical bone is associated with accumulation of microcracks with age. Bone 2000;26:375–80.
[53] Currey JD, Shahar R. Cavities in the compact bone in tetrapods and fish and their effect on mechanical properties. J Struct Biol 2013;183:107–22.